Topics in Catalysis (2019) 62:849–858
https://doi.org/10.1007/s11244-019-01167-0

ORIGINAL PAPER

Pt–Ga Model SCALMS on Modified HOPG: Growth and Adsorption Properties

Chantal Hohner[1] · Miroslav Kettner[1] · Corinna Stumm[1] · Christian Schuschke[1] · Matthias Schwarz[1] · Jörg Libuda[1,2]

Published online: 1 April 2019

Abstract
Single atom catalysts hold a great potential in heterogeneous catalysis. In this model study, we report on the observation of Pt single atoms in low-melting-point Pt–Ga alloy prepared on modified highly oriented pyrolytic graphite (HOPG) under ultrahigh vacuum (UHV) conditions. In the first part, we examined the growth of Pt nanoparticles (NP) on HOPG modified by Ar^+ bombardment. In the second part, we used physical vapor co-deposition of Pt and Ga to prepare model systems for supported catalytically active liquid metal solutions. We employed infrared reflection absorption spectroscopy with CO as a probe molecule and atomic force microscopy to study the growth and adsorption properties of Pt–Ga aggregates in comparison to Pt NPs. The presence of CO during Pt deposition leads to formation of ordered Pt particles mainly exposing terrace sites. On Pt–Ga nanoalloys, CO induces Pt segregation to the surface. In contrast, Ga deposition onto Pt in UHV or evaporation of small amounts of Pt onto Ga results in the formation of isolated Pt atoms on the surface of the alloy. Comparing alloys with different Pt concentrations, we show that the coordination environment around Pt influences the binding energy of the adsorbed CO.

Keywords Platinum · Gallium · Highly oriented pyrolytic graphite (HOPG) · Infrared reflection absorption spectroscopy (IRAS) · Atomic force microscopy (AFM) · Supported catalytically active liquid metal solutions (SCALMS)

1 Introduction

Single atom catalysts (SACs) have recently received a lot of attention [1]. Ideally, they consist of active atoms bonded to a support material, offering a uniform chemical environment. Consequently, SACs should provide very high noble metal efficiency together with excellent control over their selectivity [2]. Practically, however, the biggest challenge is the stabilization of the active site under reaction conditions. In addition, the active sites may not be uniform because the strongest binding to the support usually occurs at defect sites or impurities of the support [1, 3]. The most commonly used substrates for SACs are oxide materials, carbon, or other metals. While binding on oxides is governed by metal-support interactions [1, 4], carbon supports and metals usually require incorporation of the active metal directly into the support structure [5, 6].

Bimetallic catalysts have already proven to be efficient for dehydrogenation of alkanes [7–9] or methanol steam reforming [10, 11]. Recently, the novel concept of so-called 'supported catalytically active liquid metal solutions'(SCALMS) was presented by Taccardi et al. [12]. Its principle relies on dilution of an active metal (Pt, Pt, Rh, Ni) in a low-melting-point metal matrix (Ga, In, Sn, Pb). The resulting alloy is liquid under the reaction conditions, and, consequently, the atoms of the active metal are very mobile. It has been shown that site isolation can efficiently prevent coking of the catalyst [12]. Simultaneously, the liquid matrix provides a very uniform environment for the active metal centers. It is believed that the active atoms occasionally appear at the surface of the liquid alloy droplet in the form of single atoms [13, 14]. In comparison to catalysts used to date,

✉ Miroslav Kettner
mira.kettner@fau.de

[1] Lehrstuhl für Physikalische Chemie II, Friedrich-Alexander-Universität Erlangen-Nürnberg, Egerlandstraße 3, 91058 Erlangen, Germany

[2] Erlangen Catalysis Resource Center and Interdisciplinary Center for Interface Controlled Processes, Friedrich-Alexander-Universität Erlangen-Nürnberg, Egerlandstraße 3, 91058 Erlangen, Germany

SCALMS showed improved stability and selectivity during dehydrogenation of alkanes or pyrolysis of methane [12, 15]. While the basic functional principles of SCALMS have been recently investigated, a deeper understanding of the interplay between the active metal and the metal basis is still lacking.

In order to enable studies of SCALMS using the methods of surface science, we aim in this work at the preparation of a model system for Pt–Ga single atom catalysts under ultrahigh vacuum (UHV) conditions. Because Ga readily alloys with other metals and is prone to oxidation, we have chosen carbon as a substrate. Carbon is among the most versatile support materials in heterogeneous catalysis and electrocatalysis [16, 17]. Carbon-based materials offer low weight in combination with excellent thermal stability and electrical conductivity. Moreover, their surface composition is variable ranging from thin, flat graphene to high surface area macroporous supports [5, 18].

As a model support in this work, we used highly oriented pyrolytic graphite (HOPG). Even though HOPG has been employed in many surface science studies [19–21], it has been rarely used for infrared reflection absorption spectroscopy (IRAS) [13, 22–28]. However, Heidberg et al. showed almost 30 years ago that HOPG fulfills the metal surface selection rule (MSSR) nearly perfectly [24]. The only disadvantage in comparison to metal substrates is a slightly lower surface intensity function and slightly different optimum angle of incidence (~ 75°). Still, we showed in our previous paper that high quality spectra can be obtained using HOPG as a substrate [13]. Regarding the growth of metal nanoparticles (NPs) on HOPG, the biggest challenge is to control the nucleation and sintering. As the interaction of atoms with clean HOPG is very weak, the surface is usually roughened before the deposition of the metal, for instance by ion bombardment [19, 20, 28]. Such treatment leads to creation of defects, which help to anchor the incoming metal atoms. In our recent work, we investigated different pretreatment procedures and their influence on the metal growth [28]. In this work, we study the growth and adsorption properties of Pt NPs and Pt–Ga nanoalloys on HOPG pretreated by Ar^+ bombardment.

We used IRAS and atomic force microscopy (AFM) to investigate the morphology and growth of Pt NPs on HOPG modified by Ar^+ bombardment. Our results suggest that Pt evaporation in a CO background leads to creation of well-ordered NPs with larger terraces and less steps as compared to growth in UHV. In the second part, we prepare a model system for Pt–Ga SCALMS on modified HOPG and explore the changes upon alloying with Ga. In contrast to previous work on Ga bimetallic systems [29, 30], we focus specifically on the regime of low noble metal concentration, which is most relevant for the SCALMS concept. While Ga evaporation on Pt in UHV leads to the appearance of Pt single atoms, the presence of CO induces Pt segregation to the surface and results in the formation of larger Pt ensembles. The dynamic changes observed on the alloy suggest that such a system can serve as a model for studying the characteristics of Pt–Ga SCALMS.

2 Experimental

The IRAS measurements were carried out in an UHV system with a base pressure of 1×10^{-10} mbar. The system is equipped with a Fourier transform infrared (FTIR) spectrometer Bruker Vertex 80v along with other sample preparation and characterization tools (e.g. metal evaporators, quadrupole mass spectrometer, low energy electron diffraction, ion gun, load lock chamber, gas inlet system, etc.). The sample holder allows for heating/cooling of the sample in the temperature range from 100 to 1300 K. The spectrometer is connected to the UHV system via differentially pumped KBr windows. Both Pt and Ga metal evaporators were installed in a geometry that allowed metal deposition while performing IR spectroscopy.

The HOPG samples (MikroMasch, ZYA, 0.4° mosaic spread) were cleaved by using the 'Scotch tape' method prior to insertion into the UHV chamber. In the UHV chamber, HOPG was briefly heated to 800 K and subsequently bombarded with Ar^+ ions (Linde, purity 5.0, 500 eV, ~ 0.5 $\mu A/cm^2$) for 1 h at an angle of incidence of approx. 45° with respect to the sample normal.

Pt was deposited using a commercial electron beam evaporator (Focus EFM3) from a Pt wire (Alfa Aesar, 99.95% purity, 1 mm in diameter) onto the HOPG substrate, which was kept at room temperature. Gallium (Alfa Aesar, 99.99999% purity) was evaporated from a pyrolytic boron nitride crucible in a second electron beam evaporator (Focus EFM3) at an angle of approx. 45° with respect to the sample normal. The evaporation rates, as determined by a quartz crystal microbalance, were 0.15–0.3 Å/min for Pt and 0.5 Å/min for Ga. For the adsorption experiments, CO (Linde, 3.7) was purified with a combination of a home-built liquid nitrogen cold trap and a commercial filter assembly (Pall Gaskleen II) before dosing.

The AFM measurements were performed ex situ after the sample preparation and IRAS measurements. We used a combined AFM/STM system (Keysight Technologies, Series 5500 AFM/SPM) equipped with a combination of active and passive noise damping. For AFM experiments, silicon cantilevers were used (Pointprobe-Plus Silicon SPM Sensor PPP-NCHR, nominal spring constant of 10–130 Nm^{-1}, resonance frequency of 204–497 kHz), and the experiments were performed in non-contact mode. AFM images were post-processed (row-aligning, data leveling) using the Gwyddion software (version 2.49) [31].

3 Results and Discussion

3.1 Pt growth on Modified HOPG

As a first step, we studied the growth of Pt on modified HOPG. Prior to any metal deposition, the surface of HOPG was modified by Ar^+ bombardment. Surface modification of HOPG roughens the surface and creates anchoring points necessary for stabilizing the deposited metal against sintering. The details of this procedure can be found in the Experimental section and in our previous publication [28]. After the Ar^+ bombardment, the HOPG sample was analyzed ex situ by AFM. Figure 1a and b shows the AFM images of the surface of HOPG after the modification. The images show roughened planes terminated by plane edges and steps. The very large surface defects observable in Fig. 1b are most probably the remnants of the 'Scotch tape' cleaving procedure, which leaves some parts of the graphite pointing upwards. Our previous STM analysis of the Ar^+-bombarded HOPG showed that the structure of the planes consists of small graphene flakes of approximately 10 nm in diameter with height difference between 0.35 and 2.5 nm [28].

Figure 1c and d shows the morphology of the Ar^+-bombarded HOPG surface after the deposition of 1.5 nm of Pt in UHV. In general, the overall morphology of the surface remains unchanged and no bigger islands are observed. This leads us to the conclusion that the surface of the Ar^+-bombarded HOPG is covered with nanometer sized Pt islands which are too small to be clearly resolved by AFM. This implies that the Pt NPs are comparable in size or smaller than the graphite flakes (< 10 nm). This agrees well with our previous findings on Pd deposition, which showed that deposition of 4.5 nm of Pd on Ar^+-bombarded HOPG leads to the formation of Pd NPs of approximately 6 nm in diameter [28].

The images in Fig. 1e and f show the surface of Ar^+-bombarded HOPG after the deposition of 4.5 nm of Ga followed by evaporation of 0.225 nm of Pt. Obviously, the morphology is dramatically changed in comparison to Fig. 1a–d. We observe approximately 15 nm wide islands with height between 1 and 5 nm. The islands appear clearly separated, and the surface is homogeneously covered by islands. The particle size can be estimated from the Ga loading and the particle density as derived from AFM. The particle density determined from the image in Fig. 1e is $6 \times 10^{11}/cm^2$. For the nominal Ga loading of 4.5 nm, we obtain average number of 38,000 Ga atoms per particle. Assuming half-spherical shape, this corresponds to an average particle diameter of approximately 14 nm, in good agreement with the AFM image in Fig. 1e.

In the next step, we studied the growth of Pt on Ar^+-bombarded HOPG by IRAS. To this aim, we applied a background pressure of CO and used the stretching frequency of adsorbed CO to examine the growth of NPs. CO is commonly used as a probe molecule to study the surface structure of metal NPs [32–35]. Figure 2a shows the characteristic CO stretching region of IR spectra measured during and after physical vapor deposition (PVD) of Pt in 1×10^{-6} mbar CO. We see that directly after the start of the Pt evaporation, two bands at 2108 and 2077 cm^{-1} emerge. The band at 2077 cm^{-1} continues to grow and gradually blue-shifts to 2093 cm^{-1} with increasing Pt loading, while the band at 2108 cm^{-1} does not shift and its intensity remains unchanged. An additional weak band appears at 1853 cm^{-1} after deposition of 2.25 Å. Its intensity peaks at a Pt loading of 6 Å, and the band does not show any shift with Pt coverage.

The results can be understood on the basis of previous studies on Pt single crystals and NPs [32–40]. The band at 2077 cm^{-1} corresponds to on-top CO on the Pt NPs [33, 34]. The weak band at 2108 cm^{-1} is attributed to on-top CO adsorbed on Pt atoms modified by co-adsorption of carbon. The interaction of Pt atoms with Ar^+-bombarded HOPG was demonstrated by Yang et al. [41], and the findings are also in line with our previous study of Pd growth on Ar^+-bombarded HOPG [28]. Noteworthy, this band at 2108 cm^{-1} lies above the frequency of CO on (111) terraces (2093 cm^{-1}) and below the band of CO coadsorbed with O (~2120 cm^{-1}) [35, 42, 43]. Moreover, the band disappears with further Pt deposition, i.e., when the carbon-anchored Pt atoms get covered by additional Pt. With increasing Pt loading, the NPs get larger and their surface becomes dominated by (111) planes which feature both on-top and bridge-bonded (1853 cm^{-1}) CO [36]. Concurrently, the dipole coupling gradually shifts the on-top band to 2093 cm^{-1} [37, 38, 44].

In the next experiment, 15 Å of Pt was evaporated onto Ar^+-bombarded HOPG in UHV and subsequently exposed in several steps to CO (see Fig. 2b). IR spectra were recorded after each step. One spectrum was recorded at a CO pressure of 1×10^{-6} mbar as well. Finally, we performed a temperature programmed IRAS (TP-IRAS) measurement between 303 and 663 K in 1×10^{-6} mbar CO (2 K/min, see Fig. 2c). We observe that the on-top CO band appears initially at 2058 cm^{-1} and blue-shifts with CO exposure. No specific features are observed in the on-top CO region, which often appear on facetted Pt NPs [45, 46]. The band from bridge-bonded CO remains at 1871 cm^{-1} and red-shifts only at higher coverages. In 1×10^{-6} mbar of CO, the on-top peak is observed at 2084 cm^{-1}. In comparison to Pt deposition in CO (Fig. 2a), the band from bridge-bonded CO at 1853 cm^{-1} appears much broader. During the following TP-IRAS measurement, the intensity of the CO on-top band slowly decreases, the band red-shifts to 2044 cm^{-1} and disappears around 560 K.

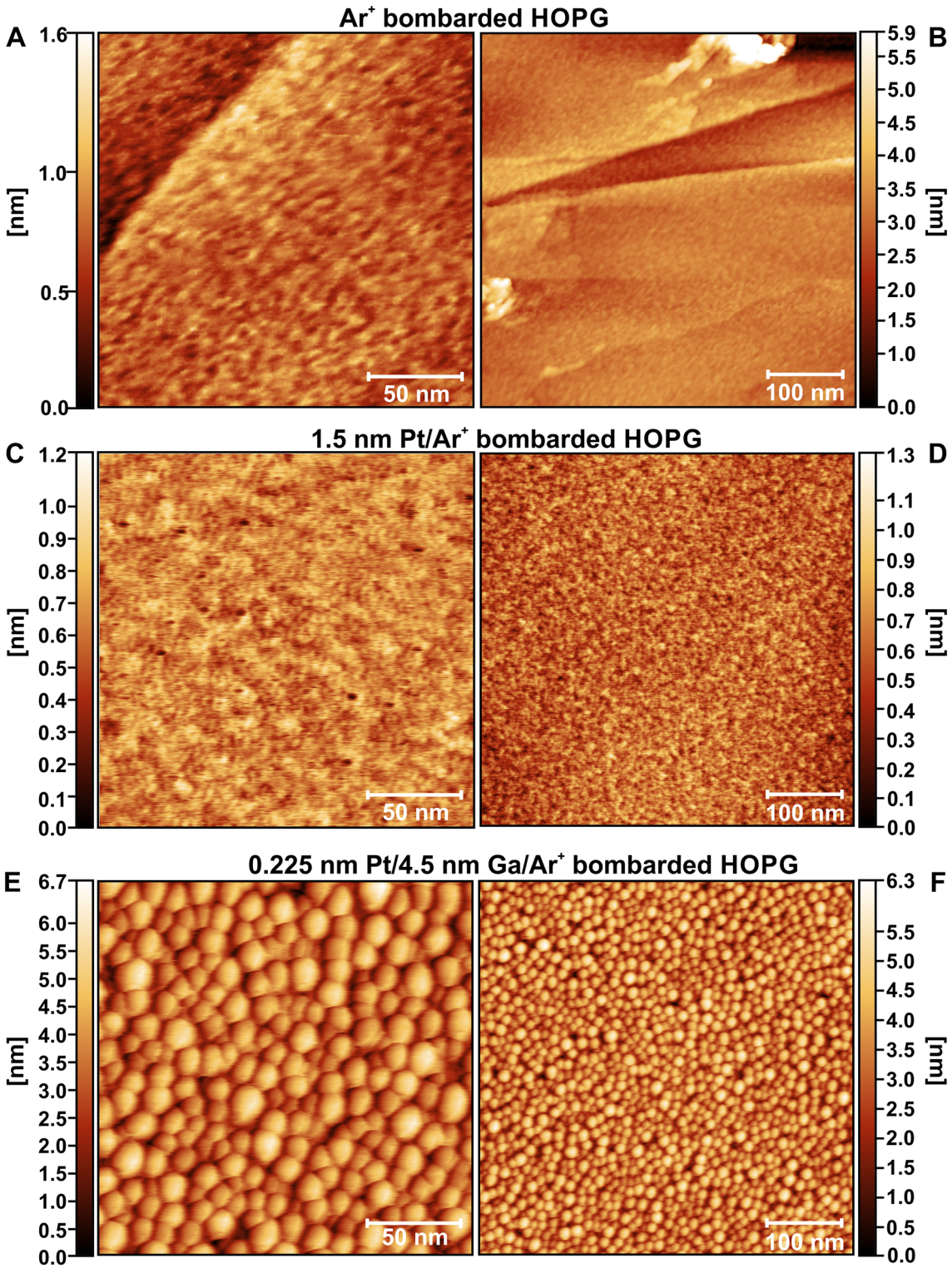

Fig. 1 AFM images of **a**, **b** HOPG modified by Ar^+ bombardment; **c**, **d** 1.5 nm Pt on Ar^+-bombarded HOPG; **e**, **f** 0.225 nm Pt on 4.5 nm Ga predeposited on Ar^+-bombarded HOPG

During the CO adsorption steps (Fig. 2b), the appearance of the CO on-top band prior to CO exposure is caused by adsorption traces of residual CO from the background. The lower initial wavenumber is attributed to reduced dipole–dipole coupling at low CO coverage and to preferential occupation of low-coordinated defect sites [44]. The

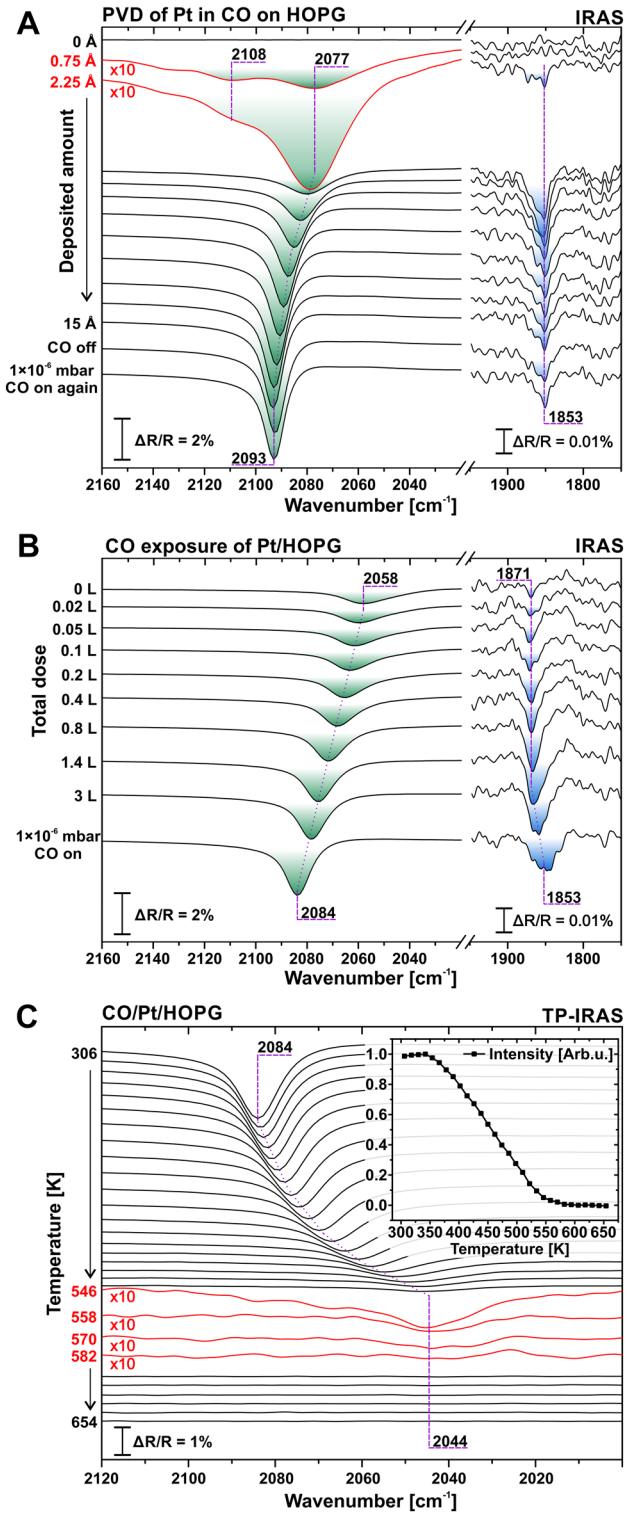

Fig. 2 **a** IR spectra taken at 300 K in CO (1×10^{-6} mbar) during Pt deposition (maximum nominal Pt coverage 1.5 nm) onto Ar^+-bombarded HOPG. **b** IR spectra recorded at 300 K during stepwise CO adsorption on Pt NPs (nominal Pt coverage 1.5 nm) deposited on Ar^+-bombarded HOPG. **c** Temperature programmed IR spectra recorded during annealing of the sample from **b** in 1×10^{-6} mbar CO. Inset shows integrated area of the peak in **c** as a function of temperature

differences observed between Pt growth in CO atmosphere and in UHV (Fig. 2a vs. Fig. 2b) suggest that Pt growth in UHV leads to the formation of defect-rich particles. As a result, a broad range of step, edge and defect sites leads to broadening of the CO band [47]. Simultaneously, the lack of long range coupling on terraces leads to a weaker blue shift as compared to Pt(111), as also observed for supported Pt NPs on SiO_2 or Al_2O_3 [44, 47, 48]. During the following TP-IRAS, the red shift and decrease in intensity between 340 and 560 K is ascribed to CO desorption. The broad range of desorption temperatures and the presence of CO up to high temperatures corroborates the heterogeneity of the Pt NPs.

3.2 Ga/Pt and Pt/Ga on Ar^+ Bombarded HOPG

In the next step, we studied the growth of Ga on Pt NPs predeposited on Ar^+-bombarded HOPG. First, 15 Å of Pt were deposited in 1×10^{-6} mbar CO on Ar^+-bombarded HOPG. Next, Ga was deposited in a CO background pressure of 1×10^{-6} mbar while continuously recording IR spectra (see Fig. 3a and b). Initially, the IR spectrum of CO on the Pt NPs shows an on-top band at 2092 cm^{-1} and a bridge band at 1855 cm^{-1}. Immediately after starting the Ga deposition, the bridge band disappears completely. Surprisingly, the overall area of the CO on-top band increases and the band becomes narrower. At a Ga/Pt ratio of 0.5, the area of the CO on-top band reaches a maximum, and, simultaneously, the width of the band is minimal. Upon further Ga deposition, the band broadens and red-shifts to 2059 cm^{-1}. After switching the CO off, the area of the CO on-top band remains unchanged.

As discussed above, the initial spectrum of the Pt NPs grown in CO indicates the formation of ordered Pt NPs predominantly terminated by (111) facets (compare Fig. 2a). The sudden disappearance of the bridge bonded CO can be explained by Ga adsorption on steps and terraces, disrupting the ensembles of Pt surface atoms. Disappearance of bridge bonded CO was previously observed on Pd–Ga and Pd–Zn alloys as well [10, 11, 13, 30]. Most probably, Ga preferentially fills defect sites and readily forms a relatively uniform surface alloy. As the surface becomes more homogeneous, the band becomes narrower and the peak intensity increases.

An increase in CO intensity upon annealing was previously observed on Pt NPs as well [49, 50]. While Barth et al. suggested that the effects may be caused by conversion of bridge bonded to linear bonded CO [49], Bourane et al. attributed the effect to a reconstruction of the Pt surface in the presence of CO [50]. In our case, the effect is induced by Ga deposition. This is not surprising, taking into account that the CO saturation coverage of Pt(111) is around 0.5 [40, 51]. Ga deposition leads to a decreasing number of Pt surface sites, but, simultaneously, to an increasing overall particle size. At low Ga loading, the increasing surface area can give rise to an increasing number of adsorbed CO

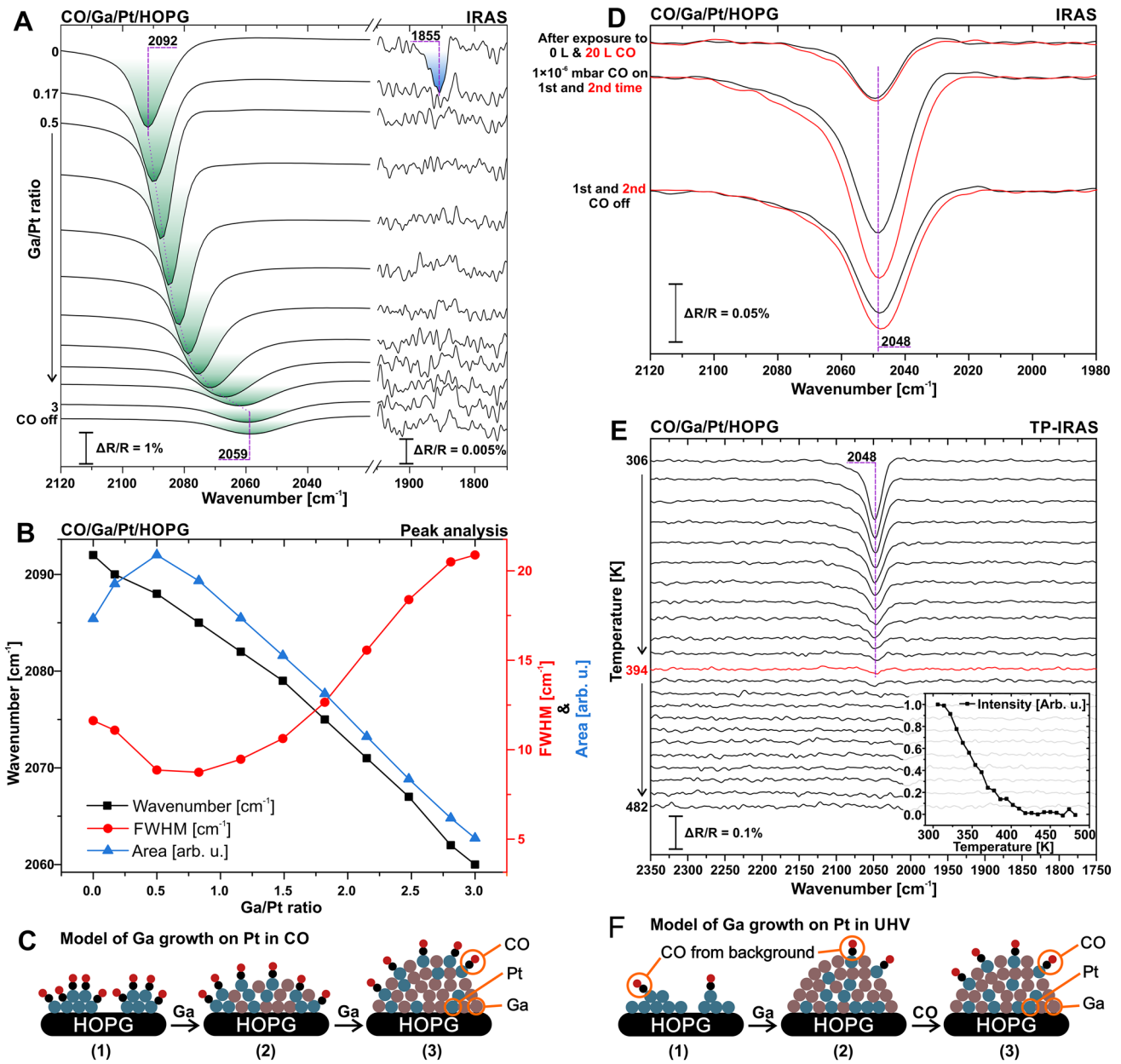

Fig. 3 **a** IR spectra of CO recorded during deposition of Ga (maximum nominal Ga coverage 45 Å) onto Pt NPs (15 Å) predeposited on Ar^+-bombarded HOPG (300 K, in 1×10^{-6} mbar CO). **b** Analysis of the CO on-top band from **a** as a function of the Ga loading. **c** Schematic representation of Ga deposition on Pt NPs in CO. **d** IR spectra acquired during exposure of a Ga-Pt nanoalloy to CO. The Pt-Ga nanoalloy was prepared in UHV by deposition of 45 Å Ga onto 15 Å Pt pre-deposited onto Ar^+-bombarded HOPG at 300 K. **e** Temperature programmed IRAS data of CO adsorbed on the sample from **d** obtained during annealing of the sample in 1×10^{-6} mbar CO. The inset shows the integrated area of the CO band from **e**. **f** Schematic representation of Ga growth on Pt NPs in UHV and subsequent CO exposure

molecules, assuming that on the nanoalloy a larger fraction of the surface Pt atoms binds to CO molecules.

With increasing Ga loading, the environment around Pt atoms changes, and the number of neighboring Pt drops. As a result, the CO on-top band shows a gradual red shift. The red shift arises from a combination of electronic ligand effects and the loss of dipole coupling. A similar deposition experiment for Pd led to a red shift of only ~ 15 cm^{-1} [13]. This difference is attributed to the weaker dipole coupling of on-top CO on Pd, where on-top sites are less favorable, and, consequently, the initial density of on-top CO is lower. The band position in the limit of high Pt dilution agrees well with recent experiments on real SCALMS. Bauer et al. showed that upon annealing of a $Ga_{37}Pt$ SCALMS to 673 K, the CO

on-top peak appeared at 2056 cm^{-1} in excellent agreement with the present data [52].

Next, we investigated a sample prepared by deposition of Ga (45 Å) onto Pt (15 Å) in UHV. In Fig. 3d, IR spectra of the CO on-top region are shown recorded after subsequent CO exposure. Immediately after Ga deposition, we observe a weak CO band which we attribute to CO adsorption from the background atmosphere during Pt and Ga deposition (both deposition steps require approximately 3 h). After CO exposure (20 L), the peak intensity remains almost unchanged, showing that the few residual Pt surface sites are already covered by CO. After raising the pressure to 1×10^{-6} mbar CO (exposure time approximately 10 min), however, we observe a drastic increase in CO intensity. The intensity drops only slightly after switching the CO off and pumping to UHV. After repeated exposure to CO (approximate exposure time 10 min, 1×10^{-6} mbar), the band intensity increases further and also remains higher after switching off the CO. The band position is perfectly constant at 2048 cm^{-1}.

This behavior is very similar to that observed on Pd–Ga model SCALMS [13]. Here we proposed that, initially, the surface of Pd–Ga NPs is Pd-free and that CO adsorption occurs at Pd atoms which appear occasionally at the surface because of diffusion. Calculations showed that the surface of Pd–Ga particles is depleted from Pd, while Pd preferentially resides in the second layer [12, 14]. Our present data suggest a very similar behavior for the Pt–Ga nanoalloys. Therefore, we ascribe the CO on-top band at 2048 cm^{-1} to CO adsorbed on Pt single atoms in a Ga environment. This assignment is corroborated by the observation that the CO stretching band shows no shifts. The absence of a coverage dependent shift suggests that the density of the adsorbed CO is so low that dipole coupling effects are negligible. At low temperature, the dynamics of the Pt–Ga nanoalloy is still relatively slow, explaining why a prolonged CO exposure is required to induce the appearance of the band.

The dynamics of the Pt–Ga nanoalloy can also explain the differences observed for the samples prepared in CO and in UHV (compare Fig. 3a and d). Because of the high binding energy of on-top CO, Pt is held at the surface during Ga deposition if sufficient amounts of CO are present. Noteworthy, no such peak was observed for Pd–Ga after the deposition of Ga, where adsorption of on-top CO is weaker [13]. Consequently, Ga deposition on Pt in the presence of CO results in a higher stabilization of Pt in the surface layer as compared to Pd.

The stretching frequency of CO is also influenced by the coordination environment. In general, the CO frequency decreases with decreasing coordination number, and, for isolated species, the on-top band is strongly red-shifted in comparison to bulk Pt [53–56]. Still, the wavenumbers differ for different substrates. As shown for Pd–Ga [21], a higher concentration of noble metal atoms in the vicinity of the Pd surface atoms lead to a higher binding energy and a higher CO stretching frequency.

For the experiments in which Ga was deposited as a second metal in UHV (Fig. 3d), there is no driving force that keeps Pt at the surface, which results in a small amount of widely separated Pt single atoms with mainly Ga atoms in their vicinity. Schematic models illustrating the growth and composition of the Pt–Ga nanoalloys are depicted in Fig. 3c and f.

Next, we recorded a TP-IRAS experiment after annealing of the Pt–Ga sample in 1×10^{-6} mbar CO. The results are shown in Fig. 3e. We observe a single band at 2048 cm^{-1}, which steadily decreases in intensity between 310 and 390 K. The intensity decreases to 50% of its original value at a temperature of 350 K. Using the Redhead equation [57] and assuming a prefactor of 10^{13} s^{-1}, we estimate an average desorption activation energy of approximately 1.1 eV for the isolated Pt species. The sizable range of desorption temperatures is attributed to the residual heterogeneity of the system, i.e., differences in particle size and coordination environment.

In the last step, we studied the growth of Pt on Ga (nominal coverage of 45 Å) pre-deposited on Ar^+-bombarded HOPG. By reversing the order of the metal deposition, we could also follow the dependence of the CO adsorption properties on the Pt surface coverage. For Pt post-deposition, the concentration of Pt at the surface is naturally higher than in the bulk. The evolution of the CO adsorption band during the Pt evaporation in 1×10^{-6} mbar CO is depicted in Fig. 4a. The CO on-top band appears at 2053 cm^{-1} and increases in intensity up to a Pt/Ga ratio of 0.04 (1.8 Å of Pt/45 Å Ga). After that, the band further grows and gradually blue-shifts to 2063 cm^{-1}.

The absence of any shift in the initial stage of Pt deposition can be explained if we assume the formation of isolated Pt atoms in a Ga matrix. At low concentration the Pt atoms do not interact, and adsorbed CO shows hardly any dipole coupling. As the Pt surface concentration increases, the distance between Pt atoms decreases, and dipole coupling effects between adjacent CO become more prominent. Also, the coordination environment of the surface Pt atoms gradually changes. Both these effects result in the observed blue shift.

For the corresponding TP-IRAS measurements, we prepared a new sample in UHV with a final Pt/Ga ratio of 0.1 and nominal coverage of 1.5 Å of Pt and 15 Å of Ga. In order to stabilize the sample against morphological changes or gradual Pt dilution, the sample was briefly preheated to 473 K in UHV. Thereafter, the TP-IRAS spectra were collected in 1×10^{-6} mbar CO (see Fig. 4b). The observed CO on-top band is located at 2051 cm^{-1} and does not shift with increasing temperature. In comparison to the previous

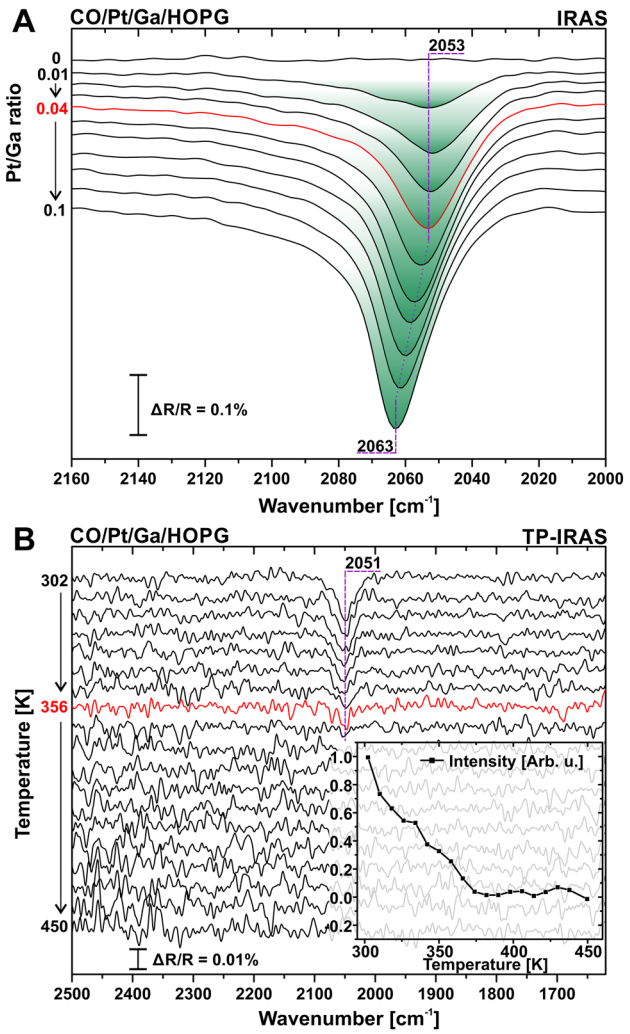

Fig. 4 **a** IR spectra recorded during deposition of Pt in CO (300 K, 1×10^{-6} mbar) onto Ga NPs (45 Å) pre-deposited onto Ar^+-bombarded HOPG. **b** Temperature programmed IRAS experiment in 1×10^{-6} mbar CO for a pre-annealed Pt–Ga nanoalloy sample. The Pt–Ga nanoalloy was prepared by deposition of 1.5 Å Pt onto 15 Å Ga pre-deposited on Ar^+-bombarded HOPG and subsequent annealing to 473 K

TP-IRAS experiment (Fig. 3e), the intensity is approximately ten times smaller. We observe that the CO band gradually decreases between 300 and 360 K. An estimate of the desorption activation energy based on the Redhead formula [57] yields a value of 1.0 eV ± 0.1 eV (for a desorption temperature of 330 ± 30 K and a heating rate of 1 K/s). The value is slightly lower than for the experiment discussed above (see Fig. 3). We attribute the differences to the different degree of Pt dilution that results from the two preparation methods. The value calculated from the data shown in Fig. 4 is considered to correspond to the limit of high Pt dilution. The adsorption energy of CO on single Pt atoms in Ga is very similar to the adsorption energy reported for Pd single atoms in Ga [13]. This is brought about by the isolation of Pt atoms and the related modification of the electronic structure of Pt atoms as demonstrated by the red shift of the CO on-top band upon alloying with Ga (see Fig. 3).

4 Conclusion

We have studied the growth and the CO adsorption properties of Pt NPs and Pt–Ga nanoalloys on HOPG modified by Ar^+ bombardment. The results from in situ IRAS studies in UHV and ex situ AFM can be summarized as follows:

1. Pt NPs grown at 300 K in the presence of 1×10^{-6} mbar CO are mainly terminated by ordered (111) terraces. In contrast, Pt NPs grown in UHV reveal a less ordered surface and a higher density of defect sites. The corresponding IR spectra show a single CO on-top band blue-shifting with increasing Pt loading.
2. Ga deposition in CO atmosphere (10^{-6} mbar) onto pre-deposited Pt NPs leads to the formation of a homogeneously modified surface, on which the adsorption in bridging sites is suppressed. At higher Ga loading, the dilution of surface Pt results in a suppression of dipole coupling and in a modification of the electronic structure of surface Pt, giving rise to a pronounced red shift of the stretching band of on-top CO. The Pt–Ga nanoalloy is dynamic already at room temperature. Exposure to CO during Ga evaporation results in an increased concentration of Pt at the surface.
3. Ga deposition onto Pt in UHV leads to the formation of nanoalloys the surface of which is fully covered by Ga. Subsequent exposure to CO leads to slow segregation of isolated Pt atoms to the surface of the nanoalloy. On-top CO on isolated surface Pt atoms is characterized by a CO stretching band at 2050 cm^{-1}.
4. Pt deposition onto Ga NPs at 300 K and in CO atmosphere (10^{-6} mbar) leads initially to the formation of isolated Pt atoms in a Ga matrix. Again, the isolated Pt species can be identified by an on-top band at 2050 cm^{-1}. At higher Pt loading, a blue-shifted CO band indicates the formation of interacting CO species and larger Pt ensembles.
5. Temperature programmed IR experiments show that CO desorbs from isolated surface Pt in a Ga–Pt nanoalloy in a temperature range from 300 to 360 K. From the spectroscopic data, we estimate a desorption activation energy of 1.0 ± 0.1 eV for highly diluted Pt in Ga.

Our results suggest that the high activity and selectivity of Pt–Ga dehydrogenation catalysts [7–9] is caused by the isolation of the surface Pt atoms and the associated modification of the electronic structure of Pt atoms as evidenced by

the red shift of the CO on-top band and the lower adsorption energy of CO. The resistance towards coking is a consequence of the structural dynamics of the Pt–Ga nanoalloy which is already observed at room temperature.

Acknowledgements This project was financially supported by the Deutsche Forschungsgemeinschaft (DFG). In particular we acknowledge support by the DFG from the Excellence Cluster 'Engineering of Advanced Materials' (Bridge Funding).

References

1. Liu J (2017) Catalysis by supported single metal atoms. ACS Catal 7:34–59. https://doi.org/10.1021/acscatal.6b01534
2. Liang S, Hao C, Shi Y (2015) The power of single-atom catalysis. ChemCatChem 7:2559–2567. https://doi.org/10.1002/cctc.201500363
3. Wang A, Li J, Zhang T (2018) Heterogeneous single-atom catalysis. Nat Rev Chem 2:65–81. https://doi.org/10.1038/s41570-018-0010-1
4. Lykhach Y, Bruix A, Fabris S et al (2017) Oxide-based nanomaterials for fuel cell catalysis: the interplay between supported single Pt atoms and particles. Catal Sci Technol 7:4315–4345. https://doi.org/10.1039/C7CY00710H
5. Li H, Zhang H, Yan X et al (2018) Carbon-supported metal single atom catalysts. New Carbon Mater 33:1–11. https://doi.org/10.1016/S1872-5805(18)60322-1
6. Kyriakou G, Boucher MB, Jewell AD et al (2012) Isolated metal atom geometries as a strategy for selective heterogeneous hydrogenations. Science 335:1209–1212. https://doi.org/10.1126/science.1215864
7. Im J, Choi M (2016) Physicochemical stabilization of Pt against sintering for a dehydrogenation catalyst with high activity, selectivity, and durability. ACS Catal 6:2819–2826. https://doi.org/10.1021/acscatal.6b00329
8. Redekop EA, Galvita VV, Poelman H et al (2014) Delivering a modifying element to metal nanoparticles via support: Pt-Ga alloying during the reduction of Pt/Mg(Al, Ga)Ox catalysts and its effects on propane dehydrogenation. ACS Catal 4:1812–1824. https://doi.org/10.1021/cs500415e
9. Sattler JJHB, Gonzalez-Jimenez ID, Luo L et al (2014) Platinum-promoted Ga/Al_2O_3 as highly active, selective, and stable catalyst for the dehydrogenation of propane. Angew Chemie Int Ed 53:9251–9256. https://doi.org/10.1002/anie.201404460
10. Föttinger K, Rupprechter G (2014) In situ spectroscopy of complex surface reactions on supported Pd–Zn, Pd–Ga, and Pd(Pt)–Cu nanoparticles. Acc Chem Res 47:3071–3079. https://doi.org/10.1021/ar500220v
11. Haghofer A, Föttinger K, Girgsdies F et al (2012) In situ study of the formation and stability of supported Pd_2Ga methanol steam reforming catalysts. J Catal 286:13–21. https://doi.org/10.1016/j.jcat.2011.10.007
12. Taccardi N, Grabau M, Debuschewitz J et al (2017) Gallium-rich Pd–Ga phases as supported liquid metal catalysts. Nat Chem 9:862–867. https://doi.org/10.1038/nchem.2822
13. Kettner M, Maisel S, Stumm C et al (2019) Pd-Ga model SCALMS: characterization and stability of Pd single atom sites. J Catal 369:33–46. https://doi.org/10.1016/j.jcat.2018.10.027
14. Grabau M, Erhard J, Taccardi N et al (2017) Spectroscopic observation and molecular dynamics simulation of Ga surface segregation in liquid Pd-Ga alloys. Chem-A 23:17701–17706. https://doi.org/10.1002/chem.201703627
15. Upham DC, Agarwal V, Khechfe A et al (2017) Catalytic molten metals for the direct conversion of methane to hydrogen and separable carbon. Science 921:917–921. https://doi.org/10.1126/science.aao5023
16. Rodríguez-Reinoso F (1998) The role of carbon materials in heterogeneous catalysis. Carbon NY 36:159–175. https://doi.org/10.1016/S0008-6223(97)00173-5
17. Mao X, Rutledge GC, Hatton TA (2014) Nanocarbon-based electrochemical systems for sensing, electrocatalysis, and energy storage. Nano Today 9:405–432. https://doi.org/10.1016/j.nantod.2014.06.011
18. Lee J, Kim J, Hyeon T (2006) Recent progress in the synthesis of porous carbon materials. Adv Mater 18:2073–2094. https://doi.org/10.1002/adma.200501576
19. Favaro M, Agnoli S, Perini L et al (2013) Palladium nanoparticles supported on nitrogen-doped HOPG: a surface science and electrochemical study. Phys Chem Chem Phys 15:2923. https://doi.org/10.1039/c2cp44154c
20. Yang DQ, Sacher E (2002) Ar^+-induced surface defects on HOPG and their effect on the nucleation, coalescence and growth of evaporated copper. Surf Sci 516:43–55. https://doi.org/10.1016/S0039-6028(02)02065-4
21. Faisal F, Toghan A, Khalakhan I et al (2015) Characterization of thin CeO_2 films electrochemically deposited on HOPG. Appl Surf Sci 350:142–148. https://doi.org/10.1016/j.apsusc.2015.01.198
22. Bolina AS, Wolff AJ, Brown WA (2005) Reflection absorption infrared spectroscopy and temperature-programmed desorption studies of the adsorption and desorption of amorphous and crystalline water on a graphite surface. J Phys Chem B 109:16836–16845. https://doi.org/10.1021/jp0528111
23. Bolina AS, Wolff AJ, Brown WA (2005) Reflection absorption infrared spectroscopy and temperature programmed desorption investigations of the interaction of methanol with a graphite surface. J Chem Phys 122:44713. https://doi.org/10.1063/1.1839554
24. Heidberg J, Warskulat M, Folman M (1990) Fourier-transform-infrared spectroscopy of carbon monoxide physisorbed on highly oriented graphite. J Electron Spectros Relat Phenom 54–55:961–970. https://doi.org/10.1016/0368-2048(90)80287-K
25. Boyd DA, Hess FM, Hess GB (2002) Infrared absorption study of physisorbed carbon monoxide on graphite. Surf Sci 519:125–138. https://doi.org/10.1016/S0039-6028(02)02207-0
26. Nalezinski R, Bradshaw AM, Knorr K (1995) Orientational phase transitions in polar physisorbed molecules: an IRAS study of dichlorodifluoromethane on graphite. Surf Sci 331–333:255–260. https://doi.org/10.1016/0039-6028(95)00227-8
27. Nalezinski R, Bradshaw AM, Knorr K (1997) A vibrational spectroscopy study of the orientational ordering in CH_3Cl monolayers physisorbed on graphite. Surf Sci 393:222–230. https://doi.org/10.1016/S0039-6028(97)00588-8
28. Kettner M, Stumm C, Schwarz M et al (2019) Pd model catalysts on clean and modified HOPG: growth, adsorption properties, and stability. Surf Sci 679:64–73. https://doi.org/10.1016/j.susc.2018.08.022
29. Kovnir K, Armbrüster M, Teschner D et al (2007) A new approach to well-defined, stable and site-isolated catalysts. Sci Technol Adv Mater 8:420–427. https://doi.org/10.1016/j.stam.2007.05.004
30. Prinz J, Gaspari R, Stöckl QS et al (2014) Ensemble effect evidenced by CO adsorption on the 3-fold PdGa surfaces. J Phys Chem C 118:12260–12265. https://doi.org/10.1021/jp501584f
31. Nečas D, Klapetek P (2012) Gwyddion: an open-source software for SPM data analysis. Cent Eur J Phys 10:181–188. https://doi.org/10.2478/s11534-011-0096-2
32. Greenler RG, Brandt RK (1995) The origins of multiple bands in the infrared spectra of carbon monoxide adsorbed on metal surfaces. Colloids Surf A 105:19–26. https://doi.org/10.1016/0927-7757(95)03336-X

33. Haneda M, Watanabe T, Kamiuchi N, Ozawa M (2013) Effect of platinum dispersion on the catalytic activity of $Pt/Al_2O_3$for the oxidation of carbon monoxide and propene. Appl Catal B 142–143:8–14. https://doi.org/10.1016/j.apcatb.2013.04.055
34. Lundwall MJ, McClure SM, Goodman DW (2010) Probing terrace and step sites on Pt nanoparticles using CO and ethylene. J Phys Chem C 114:7904–7912. https://doi.org/10.1021/jp9119292
35. Primet M (1984) Electronic transfer and ligand effects in the infrared spectra of adsorbed carbon monoxide. J Catal 88:273–282. https://doi.org/10.1016/0021-9517(84)90003-4
36. Steininger H, Lehwald S, Ibach H (1982) On the adsorption of CO on Pt (111). Surf Sci 123:264–282. https://doi.org/10.1016/0039-6028(82)90328-4
37. Kung KY, Chen P, Wei F et al (2000) Sum-frequency generation spectroscopic study of CO adsorption and dissociation on Pt(111) at high pressure and temperature. Surf Sci 463:627–633. https://doi.org/10.1016/S0039-6028(00)00639-7
38. Klünker C, Balden M, Lehwald S, Daum W (1996) CO stretching vibrations on Pt(111) and Pt(110) studied by sum-frequency generation. Surf Sci 360:104–111. https://doi.org/10.1016/0039-6028(96)00638-3
39. Tüshaus M, Schweizer E, Hollins P, Bradshaw AM (1987) Yet another vibrational study of the adsorption system Pt{111}-CO. J Electron Spectros Relat Phenom 44:305–316. https://doi.org/10.1016/0368-2048(87)87031-7
40. Hayden BE, Bradshaw AM (1983) The adsorption of CO on Pt(111) studied by infrared-reflection-adsorption spectroscopy. J Electron Spectros Relat Phenom 30:51. https://doi.org/10.1016/0368-2048(83)85033-6
41. Yang DQ, Zhang GX, Sacher E et al (2006) Evidence of the interaction of evaporated Pt nanoparticles with variously treated surfaces of highly oriented pyrolytic graphite. J Phys Chem B 110:8348–8356. https://doi.org/10.1021/jp060513d
42. Primet M, Basset JM, Mathieu MV, Prettre M (1973) Infrared study of CO adsorbed on Pt Al_2O_3. A method for determining metal-adsorbate interactions. J Catal 29:213–223. https://doi.org/10.1016/0021-9517(73)90225-X
43. Jin T, Zhou Y, Mains GJ, White JM (1987) Infrared and x-ray photoelectron spectroscopy study of carbon monoxide and carbon dioxide on platinum/ceria. J Phys Chem 91:5931–5937. https://doi.org/10.1021/j100307a023
44. Fox SG, Browne VM, Hollins P (1990) Correlated infrared studies of platinum single crystals and supported catalysts. J Electron Spectros Relat Phenom 54–55:749–758. https://doi.org/10.1016/0368-2048(90)80267-E
45. Sobota M, Happel M, Amende M et al (2011) Ligand effects in SCILL model systems: site-specific interactions with Pt and Pd nanoparticles. Adv Mater 23:2617–2621. https://doi.org/10.1002/adma.201004064
46. Brandt RK, Hughes MR, Bourget LP et al (1993) The interpretation of CO adsorbed on $Pt/SiO_2$of two different particle-size distributions. Surf Sci 286:15–25. https://doi.org/10.1016/0039-6028(93)90552-U
47. Podkolzin SG, Shen J, De Pablo JJ, Dumesic JA (2000) Equilibrated adsorption of CO on silica-supported Pt catalysts. J Phys Chem B 104:4169–4180. https://doi.org/10.1021/jp993833o
48. Hollins P (1992) The influence of surface defects on the infrared spectra of adsorbed species. Surf Sci Rep 16:51–94. https://doi.org/10.1016/0167-5729(92)90008-Y
49. Barth R, Pitchai R (1989) Thermal desorption-infrared study of carbon monoxide adsorption by alumina-supported platinum. J Catal 70:61–70. https://doi.org/10.1016/0021-9517(89)90075-4
50. Bourane A, Dulaurent O, Bianchi D (2000) Heats of adsorption of linear and multibound adsorbed CO species on a Pt/Al_2O_3catalyst using in situ infrared spectroscopy under adsorption equilibrium. J Catal 196:115–125. https://doi.org/10.1006/jcat.2000.3030
51. Ertl G, Neumann M, Streit KM (1977) Chemisorption of CO on the Pt(111) surface. Surf Sci 64:393–410. https://doi.org/10.1016/0039-6028(77)90052-8
52. Bauer T, Maisel S, Blaumeiser D, et al (2019) Operando DRIFTS and DFT study of propane dehydrogenation over solid- and liquid-supported Ga_xPt_y catalysts. ACS Catal 9:2842–2853. https://doi.org/10.1021/acscatal.8b04578
53. Therrien AJ, Hensley AJR, Marcinkowski MD et al (2018) An atomic-scale view of single-site Pt catalysis for low-temperature CO oxidation. Nat Catal 1:192–198. https://doi.org/10.1038/s41929-018-0028-2
54. Qiao B, Wang A, Yang X et al (2011) Single-atom catalysis of CO oxidation using Pt_1/FeOx. Nat Chem 3:634–641. https://doi.org/10.1038/nchem.1095
55. Moses-Debusk M, Yoon M, Allard LF et al (2013) CO oxidation on supported single Pt atoms: experimental and ab initio density functional studies of CO interaction with Pt atom on θ-Al_2O_3(010) surface. J Am Chem Soc 135:12634–12645. https://doi.org/10.1021/ja401847c
56. Brummel O, Waidhas F, Faisal F et al (2016) Stabilization of small platinum Nanoparticles on Pt-CeO_2 thin film electrocatalysts during methanol oxidation. J Phys Chem C 120:19723–19736. https://doi.org/10.1021/acs.jpcc.6b05962
57. Redhead PA (1962) Thermal desorption of gases. Vacuum 12:203–211. https://doi.org/10.1016/0042-207X(62)90978-8